Published in final edited form as:

Acta Biomater. 2024 February ; 175: 123–137. doi:10.1016/j.actbio.2023.12.034.

Fibrous finite element modeling of the optic nerve head region

Mohammad R. Islam[1,2], **Fengting Ji**[1,3], **Manik Bansal**[1], **Yi Hua**[1,4], **Ian A. Sigal**[1,3,*]

[1]Department of Ophthalmology, University of Pittsburgh, Pittsburgh PA, USA

[2]Department of Mechanical Engineering, University of Texas Rio Grande Valley, Edinburg TX, USA

[3]Department of Bioengineering, University of Pittsburgh, Pittsburgh PA, USA

[4]Department of Biomedical Engineering, University of Mississippi, MS, USA

Abstract

The optic nerve head (ONH) region at the posterior pole of the eye is supported by a fibrous structure of collagen fiber bundles. Discerning how the fibrous structure determines the region biomechanics is crucial to understand normal physiology, and the roles of biomechanics on vision loss. The fiber bundles within the ONH structure exhibit complex three-dimensional (3D) organization and continuity across the various tissue components. Computational models of the ONH, however, usually represent collagen fibers in a homogenized fashion without accounting for their continuity across tissues, fibers interacting with each other and other fiber-specific effects in a fibrous structure. We present a fibrous finite element (FFE) model of the ONH that incorporates discrete collagen fiber bundles and their histology-based 3D organization to study ONH biomechanics as a fibrous structure. The FFE model was constructed using polarized light microscopy data of porcine ONH cryosections, representing individual fiber bundles in the sclera, dura and pia maters with beam elements and canal tissues as continuum structures. The FFE model mimics the histological in-plane orientation and width distributions of collagen bundles as well as their continuity across different tissues. Modeling the fiber bundles as linear materials, the FFE model predicts the nonlinear ONH response observed in an inflation experiment from the literature. The model also captures important microstructural mechanisms including fiber interactions and long-range strain transmission among bundles that have not been considered before. The FFE model presented here advances our understanding of the role of fibrous collagen structure in the ONH biomechanics.

Graphical Abstract

[*]**Correspondence**: Ian A. Sigal, Ph.D., Laboratory of Ocular Biomechanics, Department of Ophthalmology, University of Pittsburgh Medical Center, UPMC Mercy Pavilion, 1622 Locust Street, Rm 7.382 | Pittsburgh, PA, USA. 15219, ian@OcularBiomechanics.com, www.OcularBiomechanics.org.

Disclosures: M. R. Islam None; F. Ji, None; M. Bansal, None; Y. Hua, None; I.A. Sigal, None.

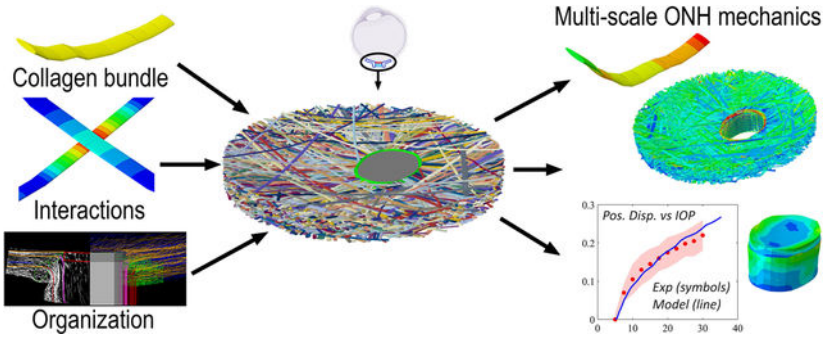

Keywords

Collagen; Fiber; Eye; Optic nerve head; Sclera; Finite element modeling; Biomechanics

1. Introduction

The optic nerve head (ONH) at the back of the eyes is a critical site where nerve damage starts in early glaucoma, especially under elevated intraocular pressure (IOP) [1–7]. In healthy eyes, the ONH region is biomechanically protected from the IOP-induced adverse effects by its collagenous tissues. These include lamina cribrosa collagen fiber bundles (called ‘beams’) within the canal [8] and a complex architecture of continuous fiber bundles in the posterior sclera, dura mater and pia mater tissues (Fig. 1). Histologically, collagen fiber bundles in the ONH region exhibit remarkable continuity among the sclera, dura mater, and pia mater tissues, forming a complex fibrous structure to support IOP (Fig. 1). While the role of collagen on the ONH biomechanics has been studied extensively, the unified effects of the collagen bundles as a fibrous structure remain elusive [4, 9, 10].

The need for a better understanding of the role of fibrous collagen structure on the ONH biomechanics is well-established [4–7, 11–19]. From the macro-to-micro perspective, it is of interest to understand how the IOP-induced macro-scale deformation is transmitted through the fibrous structure to individual fiber bundles at the micro-scale. From the micro-to-macro perspective, an in-depth knowledge of the bundle-scale deformation as modulated by local fibrous structure (i.e., organization of fiber bundles) is important to understand the microstructural basis of the macro-scale strain heterogeneity in the ONH region. Although there have been tremendous advances in recent years on experimental techniques to visualize ONH collagen fibers and their mechanics, the techniques do not yet provide information within the thick tissues with sufficient detail. Hence, computational modeling remains the most widely used approach for studying the collagen mechanics of the ONH region [3, 13, 16, 20].

Several ONH models with varying degrees of complexity in terms of macro-scale geometry and constitutive material models have been developed within the continuum finite element modeling framework of soft tissues [3, 11–13, 16, 18, 20–24]. These models assume the collagenous tissues in the ONH region to be homogenized continuum structures consisting of a soft matrix reinforced by collagen fibers. Such homogenization allows the continuum

models to predict the macro-scale ONH response efficiently with a highly simplified representation of the actual fibrous collagen structure of the ONH [3, 11, 14, 16]. However, the interpretations of the continuum model predictions must be made carefully due to the simplistic assumptions about the collagen fiber kinematics and organization [25, 26]. For example, the deformation of collagen fiber bundles is assumed independent of their interactions with the neighboring bundles in the continuum models. Histologically, however, the collagen fiber bundles are closely packed in the ONH (Fig. 1), and their interactions can critically affect the ONH biomechanics [27]. In addition, although the collagen fibers in the region are known to be continuous across tissues, the fibers in the continuum models are assumed to be non-continuous spatially (Fig. 1c). Continuum models, therefore, cannot account for a long-range transmission of forces along long fiber bundles. Andrew Voorhees and colleagues [19] developed a continuum model supplemented by long and continuous fiber bundles restricted in the coronal plane. Their models demonstrated that long fibers can cause biomechanical behaviors that are fundamentally different from those of conventional continuum models. Their models, however, were extremely simplified in geometry, for example, they were flat, without incorporating the realistic 3D organization of collagen fibers in the ONH and the interactions among fiber bundles. In summary, currently available models ONH models are limited in predicting the combined effects of long, continuous, and interacting collagen fiber bundles as a fibrous structure on the ONH biomechanics.

Our long-term goal is to understand the complex role of the fibrous collagen structure on ONH biomechanics at all levels of IOP. In this direction, we have developed a finite element modeling framework that directly incorporates discrete collagen fiber bundles, their 3D spatial organization derived from polarized light microscopy (PLM) data, interactions between fiber bundles, and long-range strain transmission along fiber bundles [28]. We have recently demonstrated that with the right hyperelastic material properties, a model can predict the nonlinear response of a small rectangular specimen, 2.00mm × 1.91mm, of the posterior sclera in biaxial tensile experiments [28].

Our goal in this work is much more ambitious. In this study we have implemented our finite element modeling approach to model a large area (10 mm × 10 mm) of collagenous tissues in the ONH region (blue region in Fig. 1a). Our finite element model efficiently incorporates the fibrous collagen fibers of the ONH region, spanning continuously across multiple layers of posterior sclera, pia mater, and dura mater tissues, mimicking the 3D histological organization of collagen fiber bundles as observed in the PLM images. We name the approach fibrous finite element (FFE) modeling to highlight its fibrous construction. We demonstrate the validity and potential of the FFE model by predicting the IOP-induced ONH response during an inflation experiment and elucidating multi-scale collagen mechanics of the ONH region.

2. Methods

In this section, we describe the FFE modeling steps in the following order. The procedure to construct model geometry is described first. Second, the finite element meshing process and the material property assignments are described. The boundary conditions and the

bundle-bundle interaction algorithm are described next. Finally, the model validation process is described in two steps consisting of structural and mechanical validation steps.

2.1 Model geometry

PLM imaging data of a porcine eye used to construct the model geometry was acquired based on our previous work [10, 28]. Details of eye preparation, histological processing, PLM imaging, and post-processing methods are described elsewhere [9, 29]. Briefly, a healthy porcine eye was obtained from the abattoir within four hours of death, then post-processed within the next four hours, and then fixed at 10% formalin for 24 hours. We use formalin for this process as it has been shown to have only minimal effects on ONH morphology, without the tissue shrinkage or distortions of other fixatives [30]. The ONH region was isolated from the fixed eye using an 11 mm circular trephine and cryo-sectioned serially in the coronal direction with a slice thickness of 30 μm. The PLM images of the coronal sections were acquired using an Olympus SZX16 microscope paired with a dual-chip Olympus DP80 camera (4.25 μm/pixel).

The construction of the model geometry involved five steps (Fig. 2). In Step 1, the collagen fiber bundles of the sclera part were constructed from multiple coronal PLM images (n=10) with pixel-level fiber orientation information. Each PLM image was post-processed first to identify the sclera region. A set of seed points (20×20), with inter-spacing of 550 μm, were selected over the PLM image to trace fiber bundles. With respect to the number of bundles, by preliminary tests, we found that a 20 × 20 grid for each PLM image provides a sufficiently dense structure with final volume fraction around 30%, within the volume fraction range (10%−60%) of sclera reported in the literature [31–34]. Further work is necessary to evaluate the role of bundle curvature and/or density. A straight fiber bundle centerline was defined at each grid point using an angle value averaged over the pixel corresponding to the grid point and its eight neighboring pixels. This process creates an assembly of fiber bundle centerlines. From this assembly, the bundle centerlines intersecting the canal were trimmed at the canal boundary and referred to as ‘radial’ fiber bundles. The remaining bundles were called ‘random’ fiber bundles in the model. It is noted that the definition of radial fiber bundles is not identical to that in our previous works, where radial fibers mean fibers organized in exact radial directions [9]. The definition of radial fiber bundles was changed as a modeling convenience to group all fiber bundles intersecting the canal with all possible angles from the periphery.

Next, the centerlines of the circumferential fiber bundles were traced following the shape of the porcine sclera canal. Briefly, we fitted an ellipse to the outer boundary of the canal and generated circumferential fiber bundles by enlarging the ellipse in the coronal plane (Fig. 2a4). The inter-spacing between two adjacent circumferential bundle centerlines was assumed to be 100 μm along both in-plane and through-thickness directions.

After tracing the centerlines of all fiber bundles, volumes were assigned to individual fiber bundles. The radial and random fiber bundles were assumed to have an elliptical cross-section with variable bundle widths sampled from the PLM-measured distribution and a constant thickness of 20 μm. We measured the widths of several bundles from the PLM images using imageJ software [35] and fitted a lognormal distribution to the measurements

(Fig. S1). We sampled bundle widths from this fitted distribution in the model. We assumed a constant thickness of 20 um for bundles based on our intuition from sagittal PLM images (Fig. 1c) in the absence of well-established literature data for this dimension in the literature. The circumferential bundles were assumed to have circular cross-sections with a constant diameter of 40 μm.

During the initial bundle tracing process from PLM images (Step 1), fiber bundles were assumed straight, but this was a transitory state where bundles are still in the coronal section plane and inter-penetrate each other. The inter-penetrations of fiber bundles were resolved as in our previous work by iteratively moving the bundle segments in the through-thickness direction [28, 36]. The process transformed the straight bundles traced from the PLM images into curved bundles with zig-zag trajectories and interwoven them with neighboring bundles. Finally, the bundles also curve when the model is compressed and shaped to match the posterior pole. Hence, the bundles when simulated were not straight. The rationale for approximating the bundles initially as straight is based on our observations from PLM where their curvature in depth is clear, but no curvature in-plane is observed. It is certainly possible that the bundles are not exactly straight, and elsewhere we have suggested that some may follow tangential “geodesic” paths [19], but the curvature was small. We posit that for this first fibrous model the reasonable agreement with the experimental orientation distributions supports the idea that the paths were also reasonable. Step 1 was repeated for multiple sections (n=10) to obtain an assembly of loosely packed fiber bundles.

In Step 2, the bundle assembly of the sclera part from the previous step was compacted with predefined displacement to reduce the sclera part thickness to 1 mm. The algorithm, used to remove inter-penetration between bundles, often moves bundles excessively (creating large gaps between bundles and crimps in the bundles) in the through-thickness direction, artificially increasing the scleral thickness beyond 1 mm. Therefore, the bundles were compressed between plates to achieve the desired thickness (Fig. 2b). The amplitude of bundle crimps in the final structure was around one to three times the bundle thickness (20 um), which is necessary to represent the interweaving architecture of the bundles. Note that these undulations are substantially larger than the conventional collagen fiber crimp, which has been reported to have median amplitude of 0.5 um [37]. This was achieved using a finite element-based algorithm [38]. Briefly, the fiber bundles were discretized using Timoshenko beam elements (1D finite element for slender structures) and dynamically compressed between two rigid plates while accounting for bundle-bundle contact interactions to prevent their interpenetrations.

In Step 3, the assembly of fiber bundles was curved by mapping the coordinates of the individual bundles over a sphere of radius, r_c = 11 mm, equal to the average internal globe radius of a porcine eye [39].

Next, in Step 4 the fiber bundles corresponding to the pia and dura mater parts were added as follows: The scleral radial fiber bundles, between 100–200 μm distance from the anterior side of the model, were extended and curved down to form the longitudinal fiber bundles of the pia mater part. A layer of circumferential fiber bundles were added adjacent to the longitudinal fiber bundles (along the nerve side), as observed histologically [9, 40]. The

scleral radial fiber bundles, 200 μm away from the anterior side of the model, were extended and curved down to form the longitudinal fiber bundles of the dura mater part [10, 41]. Based on the histological study of Raykin et al. [42], circumferential fiber bundles were added adjacent to the longitudinal fiber bundles (along the outer side) of the dura mater part.

Finally, in Step 5, the lamina cribrosa and neural tissue parts were added inside the scleral canal. Since current work focuses on the surrounding fibrous collagen structure of the ONH, both lamina cribrosa and neural tissue parts were represented as simplified continuum structures. The scleral canal was assumed to have a constant elliptical cross-section. The position of the canal was determined based on the PLM image of a middle section. To keep the model consistent with the histology, we did not move the canal or crop the model to place it at the center. A cylindrical slab with a canal-like elliptical cross-section and 100 μm thickness was added at the anterior side of the model as the lamina cribrosa part. The rest of the canal was filled with another slab as the retrolaminar neural tissue part. The lamina cribrosa and retrolaminar neural tissue parts were bonded to each other [20].

Figs. 3 and 4 show details of the entire model and its various parts. The sclera, pia mater, and dura mater parts are entirely fibrous, whereas lamina cribrosa and neural tissue parts are continuum. The sclera part of the model consists of circumferential, radial, and random fiber bundles. The pia mater and dura mater parts consist of longitudinal and circumferential fiber bundles.

Fig. 5 demonstrates the association of various fiber bundle groups of the model with their anatomic locations in the ONH region. Different anatomic sub-regions of the ONH are shown in Fig. 5a, and the fiber bundle groups associated with each anatomic sub-region considered in the model are shown in Fig. 5b. The prelaminar tissue was not considered in the model. Fig. 5c shows a cross-sectional view of the model along the sagittal plane with various fiber groups colored like the labeling in Fig. 5b. In our previous PLM-based works, we showed that the distribution of circumferential bundles is narrow near the anterior side but increases gradually with depth [10]. The distribution of circumferential fiber bundles was varied with depth in the model, consistent with the PLM data (Fig. 5d) [10]. In-plane width of circumferential bundle layers was narrow (200 μm) near the scleral canal up to 100 μm in depth from the top surface of the continuum lamina cribrosa part. The in-plane width of the circumferential bundle layers increased to 300 μm for depths between 100–400 μm. An in-plane width of 600 μm was used for the remaining circumferential fibers. Fig. 5e shows two representative collagen fiber bundles continuous from the sclera to the pia and dura maters, as observed in the PLM images. The bundles segments of each bundle in different tissues are continuous, mimicking the histological continuity of collagen fiber bundles in the ONH. Fig. 5f illustrates the qualitative comparison of the sagittal organization of collagen fiber bundles in the model and the actual tissue section as observed in a PLM image (same as Fig. 1c).

2.2 Meshing and material properties

The collagen fiber bundles were discretized using quadratic Timoshenko beam elements with an average element aspect ratio of 5. Further mesh refinement did not change the model total displacements more than 30 μm at the maximum IOP (IOP = 30 mmHg). The fiber

material was considered linear elastic with Young's modulus (E_b) and Poisson's ratio (ν_b = 0.3). Material properties were the same for all fiber bundles. E_b was used as the only material parameter for model validation. The lamina cribrosa and neural tissue parts were discretized using linear eight-nodded hexahedral elements. A linear elastic material model was used for both parts. The Young's moduli of the parts were 0.1 MPa and 0.01 MPa for the lamina cribrosa and neural tissue parts, respectively, in the same range of previous studies [2, 20].

2.3 Boundary conditions and Interactions

The model was subjected to a pressure boundary condition equivalent to IOP = 30 mmHg on the anterior side (Fig. 6a). The pressure was directly applied on the anterior surface of the lamina cribrosa. To apply the pressure boundary condition on the fibrous region, a small subset of fiber bundles was selected such that the total surface area of selected bundles is equal to the anterior surface area of the sclera part. Since beam elements are one-dimensional line elements, pressure boundary conditions cannot be applied to them. Instead, we applied a distributed force boundary condition over the length of beam elements, such that:

$$F_e = \frac{IOP \times w_e \times l_e}{l_e} = IOP \times w_e \tag{1}$$

where F_e was the applied force per unit length (l_e) of an element with width w_e, corresponding to the specified IOP. We verified the validity of this approach using a single fiber bundle model of solid elements for which pressure could be applied directly on the fiber surface and a separate model of the same fiber bundle with beam elements where the pressure was applied as a distributed force boundary condition (Fig. S2).

In addition to the pressure boundary condition, a radial displacement boundary condition (δ_r) was applied on the periphery of the model to represent the radial tension of the sclera due to IOP on the rest of the eye (Fig. 6b). The magnitude of δ_r was selected based on Laplace's law of thin-walled spherical vessels. With this assumption, the wall tension at a given IOP can be computed as:

$$T_w = \frac{IOP \times \mathrm{r_c}}{2t} \times A_w = \frac{IOP \times \mathrm{r_c}}{2\mathrm{t}} \times (\pi \mathrm{D} \times t) = \frac{IOP \times \mathrm{r_c} \times \mathrm{D}}{2} \tag{2}$$

where T_w is wall tension force and D is the diameter of the outer-most edge of the sclera part in the coronal plane (D = 11 mm). Equation (2) is satisfied by adjusting the value of δ_r for a given material parameter (E_b). In an inflation experiment, the globe is fixed far away from the ONH (near the equator or cornea), and it expands in response to the increased pressure (equivalent to IOP), causing a radial tension in the posterior sclera near the ONH. Since we are not modeling the whole eye, a radial displacement boundary condition ensures compatibility with the inflation experiments of an eye.

Bundle-to-bundle interactions were incorporated into the model using a surface-based contact algorithm similar to previous works of fiber-based models [38, 43]. The lamina cribrosa region coupled with the sclera fiber bundles by kinematically coupling the end nodes of scleral radial fiber bundles near the lamina cribrosa to the surface nodes of the lamina cribrosa (Fig. 1c). The circumferential fiber bundles of sclera and pia mater parts near the sclera canal were also kinematically coupled with the surface nodes of lamina cribrosa and neural tissue parts to ensure their mutually consistent displacement under IOP loading. In addition, the longitudinal and circumferential bundles of the dura mater were kinematically coupled to ensure that their displacement is consistent with the rest of the model. All the kinematic constraints were implemented using connector elements. The finite element solution was obtained using the commercial solver Abaqus/Explicit. An explicit solver is necessary to incorporate the contact interactions between beam elements (only available for the explicit solver). The simulations were performed in a quasi-static approach using a small time step ($\Delta t \sim 10^{-4}\ s$) to ensure the kinetic energy of the model is negligible compared to the strain energy.

2.4 Structural validation

The model structure was validated by comparing the coronal orientation and the bundle width distributions of the model with the pixel-scale fiber orientation distribution and the bundle width distribution from the PLM images (Fig. 1b). Experimental data from the PLM images were obtained using the image processing algorithms described in our previous works [28, 44].

2.5 Mechanical validation

The mechanical response of the model was validated against ex-vivo inflation experiments from the literature [45]. We compared the model predictions with the experimental measurements of the IOP-induced posterior displacements of the scleral canal and of the peripapillary sclera (PPS), and the expansion of the scleral canal. The inflation experiments were performed by increasing the IOP from 5 mmHg to 30 mmHg, and the displacements were measured using the specimen's state at 5 mmHg as the undeformed configurations. However, the ONH state at 0 mmHg was the undeformed configuration in the model, and IOP was increased from 0 to 30 mmHg. Therefore, the model predictions were shifted by 5 mmHg to ensure a one-to-one comparison of the model and experiments. The validation was performed by inversely fitting the material parameter iteratively while ensuring the applied radial displacement (δ_r) satisfied Laplace's law of Equation 2.

3. Results

3.1 Structural validation

Figure 7a compares the fiber orientation distribution in the coronal plane of the FFE model with the orientation distribution observed in the PLM images. The FFE model approximates the overall fiber orientation distribution of PLM images effectively. As expected, the coronal orientation distribution of fibers is highly isotropic in the model and the actual tissue. While the orientation distribution of the model has not been quantitatively compared for the sagittal direction, it is evident from Fig. 5f that the FFE model also qualitatively captures the sagittal

organization of collagen fiber bundles in the ONH. Fig. 7b illustrates the distributions of radial and random fiber bundle widths in the sclera as observed in the PLM images and the model. The fiber bundle width for these two groups varied over a broad range from 50 to 350 μm. In contrast, the circumferential bundles exhibited a roughly constant width of 10–20 μm.

3.2 Mechanical validation

It was found that a modulus (E_b) value of 8 MPa and a corresponding radial displacement (δ_r) of 0.1 mm allowed the FFE model to effectively capture the nonlinear variation of ONH displacements in different directions. Figure 8 shows the model-predicted average displacements (solid lines) of a porcine ONH compared to the experimental measurements of different porcine eyes (symbols) obtained from ref. [45]. The shaded regions represent the standard deviation of experimental measurements from multiple eyes (n = 12). The insets show the regions used to measure average displacements in the experiments and the model. The adjusted model predictions (blue lines) show excellent agreement with the experimental responses, for all measurements. As expected, the actual model, without adjustment (dashed grey lines), does not match the experiments as well because of the difference in reference state.

3.3 Fiber-scale mechanics of ONH

Figure 9 illustrates the deformed configurations of fibrous and continuum parts of the model with strain contour plots at normal (IOP = 15 mmHg, left column) and elevated (IOP = 30 mmHg, right column) IOP levels. Figures 9a–9b show isometric views of all the fibrous parts together, with cut-model views in Figures 9c–9d. The fibrous parts undergo highly heterogeneous strains at the bundle-scale. The bundle-scale strain along the axis of each bundle varied over a broad range from −1% to 8%. The maximum strain occurs in the circumferential fiber bundles near the lamina cribrosa for all IOP levels. While most fiber bundles undergo tensile strain, a small percentage of longitudinal fiber bundles undergo compressive strain (negative strain) due to their parallel orientation with respect to the applied IOP.

The continuum lamina cribrosa and neural tissue parts of the model suffered strains in the range from 0 to 30%. The peripheral regions of the continuum parts suffered larger strains than their core regions. The degree of strain heterogeneity was less pronounced in the continuum parts than in the fibrous parts of the model.

Fig. 10 shows the strain contour plots of various fiber bundle groups in individual fibrous parts of the model, namely the pia mater, dura mater and the sclera split by fiber group into random fibers, radial fibers and circumferential fibers. Strain was heterogeneous in all fiber bundle groups. Maximum strains occurred in the circumferential fiber bundles in all three fibrous parts. The longitudinal fiber bundles of pia and dura maters undergo relatively small strains even at elevated IOP, which is reasonable considering that the loading conditions only included IOP, and not cerebrospinal fluid pressure or gaze.

Fig. 11 shows the quantitative variation of mean bundle-level strain as a function of IOP in various fiber bundle groups of the three fibrous parts of the model. The circumferential fiber bundles suffered larger strain than the other fiber bundle groups. Interestingly, both random and radial fiber bundle groups underwent similar mean strains despite their substantially different organization in the ONH. The medians of bundle-level axial strain also exhibited similar trends for all three fibrous parts.

Fig. 12 Shows contour maps of contact stress between bundle segments at three different levels of IOP. The bundles with a contact stress less than 10 kPa are colored grey to distinguish bundles with significantly larger contact stresses, especially at elevated IOP. With the increase in IOP, the number of bundles with high contact stress (>10 kPa) increases rapidly, indicating strong interactions among bundles at elevated IOP. These interactions were particularly substantial in the ring surrounding the canal.

4. Discussion

Our goal was to develop a computational approach to directly study the biomechanics of the fibrous collagen structures in the ONH region. Our proposed FFE model has made four major advancements in studying the ONH biomechanics under elevated IOP. First, the FFE model directly incorporates histology-derived fibrous structures of long and continuous collagen fiber bundles to study ONH biomechanics as a function of its 3D collagen organization. Second, the FFE model geometrically captures the nonlinear ONH response during an inflation experiment using a simple linear elastic material model. Third, the FFE model provides a new tool to study multi-scale collagen mechanics of the ONH region. Fourth, the FFE model provides computational efficiency for the model parameter calibration and incorporates multiple deformation mechanisms of collagen bundles, such as bundle-bundle interactions and long-range strain transmission, that were not considered by previous ONH models. Each of these advancements are discussed below.

The construction of the FFE model was histology-driven and the resulting structure closely mimics the 3D organization of collagen fiber bundles in the ONH. The sclera consists of circumferential, radial, and random fiber bundles as observed in coronal PLM images [10] (Fig. 4a and Fig. 1b). The circumferential bundle distribution is depth-dependent (Fig. 5c), again similar to PLM images [10]. The pia mater part consists of longitudinal fiber bundles as observed in the sagittal PLM image (Fig. 4b and Fig. 1c). The circumferential fiber bundles are also added to the pia mater part, based on the PLM images from the retro-laminar regions and other's work [40]. The longitudinal and circumferential fiber bundles are incorporated into the dura mater part based on the histological study of the optic nerve sheath [42]. Collagen fiber bundles in the ONH region are long and continuous, crossing between tissue layers and even between tissues, for example bundles crossing between the sclera and the dura mater (Figure 5e). In conventional models, this continuity is not preserved, affecting fiber loading across tissue boundaries.

The overall bundle orientation and width distributions of the model also match those measured from the PLM images (Fig. 7). The construction of an ONH model with all these complex geometric characteristics related to 3D collagen organization in the ONH region

is a major contribution of this work. It is important to note that previous ONH models do not account for the 3D organization and continuity of collagen fiber bundles across different tissues [3, 13, 16]. The tissue-mimetic 3D collagen organization of the FFE model naturally makes the model predictions physiologically relevant and closer representations of the actual ONH biomechanics.

The FFE model captured the nonlinear response of ONH during inflation experiments by virtue of its tissue-mimetic fibrous construction. This is consistent with previous micro-scale discrete network-based models with idealized organization of fibers, which have also been shown to recapitulate soft tissue-like nonlinear stress-strain behavior [43, 46]. The FFE model can be considered as a macro-scale fiber network model that simultaneously recapitulates the tissue-mimetic organization of collagen fibers and nonlinear mechanics of the ONH. The model simultaneously predicted the nonlinear variation of peripapillary sclera's posterior displacement and scleral canal expansion with IOP (Fig. 8). The nonlinear response predicted by the FFE model was an entirely geometric effect since all the material parameters of collagen fibers, lamina cribrosa, and neural tissue were linear elastic. These results demonstrate that the nonlinear mechanical behavior of collagenous tissues in the ONH region can emerge from their nonlinear geometry rather than their bulk nonlinear material properties. The choice of a linear elastic constitutive model for collagen fibers is intuitive since bundle-level strains in the model are small in the order of 3–5% (Fig. 11). Our findings are consistent with experimental studies that have reported that single collagen fibers have a response to load that is also approximately linear in a similar strain range [47, 48].

The FFE model allows for the direct investigation of multi-scale biomechanics of the ONH region from the macro-scale fibrous collagen structures and other tissues to the single collagen fiber bundle. At the macro-scale, both the model and experimental results showed that relatively soft lamina cribrosa and neural tissue parts undergo larger posterior displacements compared to the peripapillary sclera (Fig. 8a and Fig. 8b). For example, the average posterior displacement of these two parts is approximately 0.4 mm at 30 mmHg, which is approximately two times the posterior displacement of peripapillary sclera. This is not a surprise considering that the lamina cribrosa was modeled as fairly thin, flat, and with tissue stiffness at the lower end of the range of moduli considered elsewhere [49, 50]. Sclera canal expansion was also relatively small compared to the posterior displacement of the ONH region (Fig. 8c), again helping explain the larger posterior displacements of the lamina [49].

The collagen fiber bundles of the sclera, pia mater, and dura mater experienced highly heterogeneous strains under elevated IOP (Fig. 9a–9d). At normal IOP (IOP = 15 mmHg), a large percentage of fiber bundles exhibited relatively small strains (< 1%), indicating a few bundles carried the pressure load under normal IOP (Fig. 9a and 9c). At elevated IOP (IOP = 30 mmHg), many bundles experienced comparable strain (2–5%), suggesting their involvement in carrying the excessive pressure load (Fig. 9b and 9d). These observations are consistent with studies predicting or measuring the degree of collagen fiber uncrimping and/or recruitment with IOP [51, 52]. The FFE model results elucidate that collagenous tissues in the ONH region gradually involve more fiber bundles to bear the increasing

IOP. The circumferential fiber bundles suffer a larger strain than the other bundle groups in all three fibrous parts. The circumferential bundles near the lamina cribrosa suffer the maximum strain among all fiber bundles in the model. It is likely because circumferential bundles have to prevent scleral canal expansion, and do not have much “slack”. The longitudinal fiber bundles of pia mater and dura mater parts undergo relatively small strain even at elevated IOP, implying their minimal role in supporting IOP. We suspect that applying cerebrospinal fluid pressure [23, 53–55], or forcing a change in gaze [21, 56, 57]would likely result in much larger loads on the pia and dura.

The FFE model provides several computational advancements in terms of modeling ONH biomechanics compared to conventional models of the field. The FFE model is not restricted by the assumption of a homogenized continuum structure. A major limitation of the continuum structure assumption is that collagen fibers are represented empirically as a separate constitutive phase within each solid element with a preferred orientation. The definition of collagen in a continuum model refers to the fiber phase, not a single fiber or a bundle of fibers, limiting its ability to predict individual fiber or bundle-level stress or strain fields independently. Our FFE model defines collagen as homogenized bundles of fibers (i.e., assuming all fibers in a bundle deform together). It directly captures the stress and strain fields of individual bundles and their collective response as a fibrous structure under the applied IOP.

The continuum models further assume that collagen fibers or bundles are not continuous across elements. It precludes long-range strain transmission along the lengths of bundles which would affect local stress and strain fields. For example, if we apply a stretch boundary condition to a radial fiber bundle (highlighted in red in Fig. S3a), it could have a direct action on the lamina cribrosa due to long-range strain transmission. However, the homogenized continuum model would dissipate and thus minimize the effect without a long-range strain transmission mechanism and the continuity of the fiber bundle across elements (Fig. S3b). The long-range strain transmission effect has been numerically simulated in a different scenario by Zarei and coworkers [58]. The authors simulated an axon being embedded in a collagen matrix using two modeling approaches, where one model represented the collagen matrix as a fibrous structure, and the other model used a homogenized continuum structure. They show that the continuum model significantly underestimates the axon strain compared to that in a fibrous model [58]. A similar comparison of the fibrous and continuum ONH models would be insightful but remains beyond the scope of the current work.

Another advancement enabled by our approach is the incorporation of fiber bundle-bundle interactions. These interactions give rise to localized contact stresses in the bundle segments, which can be significantly larger compared to the applied IOP (Fig. 12). For example, contact stress as large as 100 kPa (equivalent to 750 mmHg) was observed in some bundles at IOP = 30 mmHg (Fig. 12c). Such large contact stresses are partly caused by the IOP-induced compression of bundles. In addition, the geometric constraints imposed by the neighboring bundles can induce large contact stresses in a bundle to obstruct its kinematics under the applied IOP. Therefore, the kinematics of a fiber bundle depend on its interactions with the neighboring bundles, especially in regions of tightly interwoven fiber bundles.

The fiber bundle kinematics in the continuum models largely follows a stretch-controlled mechanism without being affected by neighboring bundles [13, 16]. It limits the ability of continuum models to capture physiologically-relevant fiber bundle kinematics under the applied IOP. This, in turn, points to FFE models as more likely to provide fiber stresses relevant to tissue remodeling than continuum models.

The FFE model only required iterative adjustment of one model parameter (E_b) to match the experimental response of a porcine ONH. In contrast, continuum models require an inverse finite element-based multivariate parameter optimization technique for model calibration [12]. Therefore, the FFE model is complex by geometric construction but computationally efficient in model calibration. The FFE model does not involve any phenomenological parameter, such as region-dependent preferred fiber orientation, to capture the structural anisotropy of the sclera, as used in the continuum models [13, 16]. The anisotropy of collagen organization is geometrically incorporated in the FFE model.

The FFE modeling technique has limitations that must be considered when interpreting the results, and that require further investigation. First, the model was developed based on a porcine eye and the results may not be directly applied to human eyes. However, since both porcine and human eyes share several common features, including three characteristic groups of fiber bundles in a coronal section and the continuity of scleral fiber bundles into the pia and dura mater parts, we posit that the fiber deformation mechanisms will be similar in human eyes. Future work will focus on developing FFE models of human eyes to investigate the differences in detail. Second, the FFE model was constructed from a healthy porcine eye but for model validation we used literature data from experiments performed on different porcine eyes [45]. Our FFE model predictions are still representative of the porcine ONH response since they are within the limit of experimental variability for different eyes. It will be useful to develop a specimen-specific FFE model in the future.

Third, the FFE model contained a representative volume fraction of collagen fiber bundles, which may not be the same as the actual tissue. This is limited by the computational challenge to model a large number of non-overlapping fiber bundles. In the current model, the volume fraction of collagen fiber bundles is around 30%, within the reported range of sclera volume fraction (10–60%) in previous works [31–34]. The volume fraction of fiber bundles will affect the model parameter (E_b) value required to predict the experimental response. It is unlikely to alter the deformation mechanisms of fiber bundles as observed in previous fiber-based models with different fiber volume fractions [43]. Further work is required to understand how fiber fraction affects the overall behavior of the FFE model.

Fourth, the proposed FFE model simulated the fibrous collagen structures in the ONH region without a matrix, but the collagen fiber bundles in actual tissues are embedded in a matrix. Hence, in matching an experiment in which the matrix is present, our model will overestimate slightly the fiber bundle modulus to account for the missing matrix. The effect, however, is likely to be small since it is well-established that the matrix is significantly softer than the collagen fibers in the sclera. For example, previous works reported an elastic modulus of the matrix in the order of 0.1–0.5 MPa [12, 16, 59], which is less than 5% of collagen fiber bundle modulus (E_b = 8 MPa) reported in this work.

It is important to note that our estimated collagen modulus (E_b = 8 MPa) represents bundle-scale modulus of collagen. In the PLM images of porcine sclera, we observed collagen fiber bundles with variable widths in the range from 50–350 μm (Fig. 7b) and we modeled collagen at this length-scale in this work. The bundle modulus is derived by comparing the bulk tissue behavior of the FFE model and experiment from ref. [45]. The collagen bundle properties of the FFE model do not represent bulk-scale properties of sclera, as may be used, for instance in conventional continuum models [2]. The properties also do not represent fibril-scale (~ 1 μm) properties. Most continuum ONH models represented collagen at fibril-scale and reported collagen modulus in the order of 30–1000 MPa [11, 16, 28, 60]. These differences are important as the material properties of collagen are heavily length-scale dependent [61].

In previous models of the sclera, the matrix phase is generally included as a continuum structure, and the collagen fibers are embedded in the matrix [62]. However, this approach constrains the collagen fibers significantly and forces them to deform affinely, but it is well-recognized that collagen fibers undergo nonaffine deformation in the soft tissues [62, 63]. Modeling the matrix phase without over-restricting fiber kinematics is a computationally challenging task and will be addressed in future works. Several studies have explored the roles of non-collagen elements of the matrix, such as glycosaminoglycans [64, 65], but their primary effect on sclera stiffness [66]remains controversial, and thus it remains unclear how they should be included.

Fifth, the interactions among fiber bundles in the FFE model were simulated using a frictionless contact algorithm partially due to the unavailability of experimental data on the friction coefficient of collagen fibers and computational complexity. We speculate that the frictional contribution to the overall response of a healthy ONH is small, based on previous studies [28, 67]. This could be different in the aged or diseased ONH [66]. Sixth, collagen fiber-level crimp was not considered in the current FFE model, although collagen fibers in the sclera exhibit highly crimped structures [68]. The fiber-level crimp affects the tissue response to IOP because collagen fibers must be uncrimped or recruited first to bear the IOP-induced load [69]. Our model does not account for several effects that occur at very low IOPs, such as tissue buckling or collapse, and does not account for pre-stress. Our model does not account for fiber-level crimp (it only accounts for bundle-level crimp). The effects at very low IOPs are extremely complex, and therefore even the experiment does not account for them, taking as baseline the condition at IOP=5mmHg. Hence, we believe that a fair comparison between model and experiments must be our model at an IOP=5mmHg. It explains partly why the actual tissue with crimped fibers remains undeformed even at IOP = 5 mmHg during the inflation experiments. But the FFE model with uncrimped fibers starts deforming beyond IOP =0 mmHg. In addition, the ocular shell at low pressure can also buckle and collapse, which requires a finite pressure to stabilize the ocular shell and perform the experiments. Since our model does not include the pre-stress of collagen fiber bundles, the effects of tissue buckling or collapse at very low pressures cannot be incorporated into the model. Future FFE models will benefit from incorporating fiber crimp and pre-stress [60] information to better characterize the collagen fiber mechanics of the ONH region under elevated IOP.

Seventh, although the FFE model general architecture was shown consistent with experimentally-derived structural measures of fiber orientation, the model is still an approximation. For the non-circumferential fibers, the model was built in a way that was agnostic to the type of fiber. As such, particular groups of fibers may be over or under-represented. This may be the case, for instance for radially aligned that form a thin layer on the innermost sclera [41], and for long tangential fibers that we have argued elsewhere could play a major role in scleral canal biomechanics [19]. A more detailed reconstruction of the sclera architecture could ensure that these fiber groups are fully accounted for and thus be in the position to better determine their role. Eighth, the time-dependent viscoelastic properties of the sclera were not included in the model. Understanding how tissue viscoelasticity affects ONH biomechanics under IOP requires a more detailed study, which is beyond the scope of current work.

Nineth, the optical properties that the PLM technique leverages to determine local tissue fiber orientation may be subject to artifacts in tissue locations with multiple crossing fibers. Consequently, in tissue regions with many crossing fibers, such as the sclera, local PLM fiber orientations should be treated with caution. We believe that the effects of this issue in the current model is modest given that the models focus on thicker fiber bundles (30 μm sections vs. 50–400 μm bundles widths).

Lastly, the representation of lamina cribrosa and its connection with the surrounding fibrous collagen structures were highly simplified in the current FFE model. In our previous works, we incorporated a more complex representation of lamina cribrosa microstructure in the ONH model [18, 70]. We consciously used a simplified representation of the lamina cribrosa to focus our work on the effects of surrounding fibrous collagen structures on the ONH biomechanics. In the actual tissue, the lamina cribrosa also consists of collagen fiber bundles (called beams) that form complex insertions at the periphery to establish the connection between the sclera and lamina cribrosa. The structure, mechanics, and role in pathology of lamina cribrosa insertions remain one of the least understood areas of the ocular biomechanics field and require further experimental studies to be able to model this crucial region accurately [71–73].

In conclusion, the proposed FFE model provides a high-fidelity approach for studying the previously unknown relationships between the fibrous collagen structure in the ONH region and ONH biomechanics under elevated IOP. By virtue of its histology-driven 3D fibrous construction, the FFE model provides direct access to multi-scale collagen fiber mechanics in the ONH region. It provides insights into physiologically relevant deformation mechanisms of collagen fibers through long-range strain transmission and fiber bundle-bundle interactions. In the ocular biomechanics literature, it is frequently assumed that collagen fibers reinforce the sclera as independent constituents similar to fiber-reinforced composite materials. However, in this work, we demonstrated that the reinforcement occurs through a complex fibrous structure, in which collagen fibers interact with each other and transmit forces and displacements over long-range to support IOP. Our findings demonstrate that the fibrous structure of collagen bundles has a greater role in optic nerve head biomechanics than previously recognized by the ocular biomechanics community. An in-

depth understanding of collagen mechanics potentially leveraging the fibrous finite element modeling approach will have a far-reaching impact on glaucoma diagnosis and treatment.

Supplementary Material

Refer to Web version on PubMed Central for supplementary material.

Funding:

This work was supported in part by the National Institutes of Health R01-EY023966, R01-EY028662, R01-EY031708, P30-EY008098 and T32-EY017271 (Bethesda, MD), the Eye and Ear Foundation (Pittsburgh, PA), Research to Prevent Blindness (unrestricted grant to UPMC Ophthalmology and Stein Innovation Award to IA Sigal).

References

[1]. Sigal IA, Ethier CR, Biomechanics of the optic nerve head, Experimental eye research 88(4) (2009) 799–807. [PubMed: 19217902]

[2]. Sigal IA, Flanagan JG, Ethier CR, Factors Influencing Optic Nerve Head Biomechanics, Investigative Ophthalmology & Visual Science 46(11) (2005).

[3]. Coudrillier B, Boote C, Quigley HA, Nguyen TD, Scleral anisotropy and its effects on the mechanical response of the optic nerve head, Biomechanics and modeling in mechanobiology 12 (2013) 941–963. [PubMed: 23188256]

[4]. Boote C, Sigal IA, Grytz R, Hua Y, Nguyen TD, Girard MJ, Scleral structure and biomechanics, Progress in retinal and eye research 74 (2020) 100773. [PubMed: 31412277]

[5]. Downs JC, Optic nerve head biomechanics in aging and disease, Experimental eye research 133 (2015) 19–29. [PubMed: 25819451]

[6]. Coudrillier B, Pijanka JK, Jefferys JL, Goel A, Quigley HA, Boote C, Nguyen TD, Glaucoma-related changes in the mechanical properties and collagen micro-architecture of the human sclera, PloS one 10(7) (2015) e0131396. [PubMed: 26161963]

[7]. Pijanka JK, Markov PP, Midgett D, Paterson NG, White N, Blain EJ, Nguyen TD, Quigley HA, Boote C, Quantification of collagen fiber structure using second harmonic generation imaging and two-dimensional discrete Fourier transform analysis: application to the human optic nerve head, Journal of biophotonics 12(5) (2019) e201800376. [PubMed: 30578592]

[8]. Downs JC, Roberts MD, Sigal IA, Glaucomatous cupping of the lamina cribrosa: a review of the evidence for active progressive remodeling as a mechanism, Experimental eye research 93(2) (2011) 133–140. [PubMed: 20708001]

[9]. Jan N-J, Lathrop K, Sigal IA, Collagen architecture of the posterior pole: high-resolution wide field of view visualization and analysis using polarized light microscopy, Investigative ophthalmology & visual science 58(2) (2017) 735–744. [PubMed: 28146238]

[10]. Gogola A, Jan N-J, Lathrop KL, Sigal IA, Radial and circumferential collagen fibers are a feature of the peripapillary sclera of human, monkey, pig, cow, goat, and sheep, Investigative ophthalmology & visual science 59(12) (2018) 4763–4774. [PubMed: 30304458]

[11]. Karimi A, Rahmati SM, Razaghi R, Girkin CA, Downs JC, Finite element modeling of the complex anisotropic mechanical behavior of the human sclera and pia mater, Computer Methods and Programs in Biomedicine 215 (2022) 106618. [PubMed: 35026624]

[12]. Karimi A, Rahmati SM, Grytz RG, Girkin CA, Downs JC, Modeling the biomechanics of the lamina cribrosa microstructure in the human eye, Acta Biomaterialia 134 (2021) 357–378. [PubMed: 34245889]

[13]. Grytz R, Krishnan K, Whitley R, Libertiaux V, Sigal IA, Girkin CA, Downs JC, A mesh-free approach to incorporate complex anisotropic and heterogeneous material properties into eye-specific finite element models, Computer methods in applied mechanics and engineering 358 (2020) 112654.

[14]. Zhang L, Albon J, Jones H, Gouget CL, Ethier CR, Goh JC, Girard MJ, Collagen microstructural factors influencing optic nerve head biomechanics, Investigative ophthalmology & visual science 56(3) (2015) 2031–2042. [PubMed: 25736791]

[15]. Guan C, Pease ME, Quillen S, Ling YTT, Li X, Kimball E, Johnson TV, Nguyen TD, Quigley HA, Quantitative Microstructural Analysis of Cellular and Tissue Remodeling in Human Glaucoma Optic Nerve Head, Investigative ophthalmology & visual science 63(11) (2022) 18–18.

[16]. Schwaner SA, Hannon BG, Feola AJ, Ethier CR, Biomechanical properties of the rat sclera obtained with inverse finite element modeling, Biomechanics and modeling in mechanobiology 19(6) (2020) 2195–2212. [PubMed: 32361821]

[17]. Campbell IC, Coudrillier B, Ross Ethier C, Biomechanics of the posterior eye: a critical role in health and disease, Journal of biomechanical engineering 136(2) (2014) 021005. [PubMed: 24356942]

[18]. Voorhees A, Jan N-J, Sigal I, Effects of collagen microstructure and material properties on the deformation of the neural tissues of the lamina cribrosa, Acta biomaterialia 58 (2017) 278–290. [PubMed: 28528864]

[19]. Voorhees AP, Jan N-J, Hua Y, Yang B, Sigal IA, Peripapillary sclera architecture revisited: a tangential fiber model and its biomechanical implications, Acta biomaterialia 79 (2018) 113–122. [PubMed: 30142444]

[20]. Sigal IA, Flanagan JG, Tertinegg I, Ethier CR, Finite element modeling of optic nerve head biomechanics, Investigative ophthalmology & visual science 45(12) (2004) 4378–4387. [PubMed: 15557446]

[21]. Wang X, Rumpel H, Lim WEH, Baskaran M, Perera SA, Nongpiur ME, Aung T, Milea D, Girard MJ, Finite element analysis predicts large optic nerve head strains during horizontal eye movements, Investigative ophthalmology & visual science 57(6) (2016) 2452–2462. [PubMed: 27149695]

[22]. Grytz R, Meschke G, Jonas JB, The collagen fibril architecture in the lamina cribrosa and peripapillary sclera predicted by a computational remodeling approach, Biomechanics and modeling in mechanobiology 10 (2011) 371–382. [PubMed: 20628781]

[23]. Feola AJ, Myers JG, Raykin J, Mulugeta L, Nelson ES, Samuels BC, Ethier CR, Finite element modeling of factors influencing optic nerve head deformation due to intracranial pressure, Investigative ophthalmology & visual science 57(4) (2016) 1901–1911. [PubMed: 27088762]

[24]. Girard MJ, Downs JC, Burgoyne CF, Suh J-KF, Peripapillary and posterior scleral mechanics—part I: development of an anisotropic hyperelastic constitutive model, (2009).

[25]. Stracuzzi A, Britt BR, Mazza E, Ehret AE, Risky interpretations across the length scales: continuum vs. discrete models for soft tissue mechanobiology, Biomechanics and Modeling in Mechanobiology 21(2) (2022) 433–454. [PubMed: 34985590]

[26]. Picu CR, Constitutive models for random fiber network materials: a review of current status and challenges, Mechanics Research Communications 114 (2021) 103605.

[27]. Wang B, Hua Y, Brazile BL, Yang B, Sigal IA, Collagen fiber interweaving is central to sclera stiffness, Acta biomaterialia 113 (2020) 429–437. [PubMed: 32585309]

[28]. Ji F, Bansal M, Wang B, Hua Y, Islam MR, Matuschke F, Axer M, Sigal IA, A direct fiber approach to model sclera collagen architecture and biomechanics, bioRxiv (2022) 2022.11.20.517259.

[29]. Jan N-J, Grimm JL, Tran H, Lathrop KL, Wollstein G, Bilonick RA, Ishikawa H, Kagemann L, Schuman JS, Sigal IA, Polarization microscopy for characterizing fiber orientation of ocular tissues, Biomedical optics express 6(12) (2015) 4705–4718. [PubMed: 26713188]

[30]. Tran H, Jan N-J, Hu D, Voorhees A, Schuman JS, Smith MA, Wollstein G, Sigal IA, Formalin fixation and cryosectioning cause only minimal changes in shape or size of ocular tissues, Scientific reports 7(1) (2017) 1–11. [PubMed: 28127051]

[31]. Bashkatov AN, Tuchin VV, Genina EA, Sinichkin YP, Lakodina NA, Kochubey VI, Human sclera dynamic spectra: in-vitro and in-vivo measurements, Ophthalmic Technologies IX, SPIE, 1999, pp. 311–319.

[32]. Edwards A, Prausnitz MR, Fiber matrix model of sclera and corneal stroma for drug delivery to the eye, AIChE journal 44(1) (1998) 214–225.

[33]. Grytz R, Sigal IA, Ruberti JW, Meschke G, Downs JC, Lamina cribrosa thickening in early glaucoma predicted by a microstructure motivated growth and remodeling approach, Mechanics of Materials 44 (2012) 99–109. [PubMed: 22389541]

[34]. Xia M, Zhang E, Yao F, Xia Z, Zhou M, Ran X, Xia X, Regional differences of the sclera in the ocular hypertensive rat model induced by circumlimbal suture, Eye and Vision 10(1) (2023) 2. [PubMed: 36597143]

[35]. Collins TJ, ImageJ for microscopy, Biotechniques 43(S1) (2007) S25–S30.

[36]. Matuschke F, Amunts K, Axer M, fastPLI: A Fiber Architecture Simulation Toolbox for 3D-PLI, Journal of Open Source Software 6(61) (2021) 3042.

[37]. Jan N-J, Brazile BL, Hu D, Grube G, Wallace J, Gogola A, Sigal IA, Crimp around the globe; patterns of collagen crimp across the corneoscleral shell, Experimental eye research 172 (2018) 159–170. [PubMed: 29660327]

[38]. Islam M, Tudryn GJ, Picu CR, Microstructure modeling of random composites with cylindrical inclusions having high volume fraction and broad aspect ratio distribution, Computational Materials Science 125 (2016) 309–318.

[39]. Murienne BJ, Jefferys JL, Quigley HA, Nguyen TD, The effects of glycosaminoglycan degradation on the mechanical behavior of the posterior porcine sclera, Acta biomaterialia 12 (2015) 195–206. [PubMed: 25448352]

[40]. Pijanka JK, Spang MT, Sorensen T, Liu J, Nguyen TD, Quigley HA, Boote C, Depth-dependent changes in collagen organization in the human peripapillary sclera, PloS one 10(2) (2015) e0118648. [PubMed: 25714753]

[41]. Hua Y, Voorhees AP, Jan N-J, Wang B, Waxman S, Schuman JS, Sigal IA, Role of radially aligned scleral collagen fibers in optic nerve head biomechanics, Experimental eye research 199 (2020) 108188. [PubMed: 32805265]

[42]. Raykin J, Forte TE, Wang R, Feola A, Samuels BC, Myers JG, Mulugeta L, Nelson ES, Gleason RL, Ethier CR, Characterization of the mechanical behavior of the optic nerve sheath and its role in spaceflight-induced ophthalmic changes, Biomechanics and modeling in mechanobiology 16 (2017) 33–43. [PubMed: 27236645]

[43]. Islam M, Picu R, Effect of network architecture on the mechanical behavior of random fiber networks, Journal of Applied Mechanics 85(8) (2018).

[44]. Yang B, Jan NJ, Brazile B, Voorhees A, Lathrop KL, Sigal IA, Polarized light microscopy for 3-dimensional mapping of collagen fiber architecture in ocular tissues, Journal of biophotonics 11(8) (2018) e201700356. [PubMed: 29633576]

[45]. Pavlatos E, Ma Y, Clayson K, Pan X, Liu J, Regional deformation of the optic nerve head and peripapillary sclera during IOP elevation, Investigative ophthalmology & visual science 59(8) (2018) 3779–3788. [PubMed: 30046819]

[46]. Chandran PL, Barocas VH, Affine versus non-affine fibril kinematics in collagen networks: theoretical studies of network behavior, (2006).

[47]. Shen ZL, Dodge MR, Kahn H, Ballarini R, Eppell SJ, Stress-strain experiments on individual collagen fibrils, Biophysical journal 95(8) (2008) 3956–3963. [PubMed: 18641067]

[48]. Van Der Rijt JA, Van Der Werf KO, Bennink ML, Dijkstra PJ, Feijen J, Micromechanical testing of individual collagen fibrils, Macromolecular bioscience 6(9) (2006) 697–702. [PubMed: 16967482]

[49]. Sigal IA, Yang H, Roberts MD, Grimm JL, Burgoyne CF, Demirel S, Downs JC, IOP-induced lamina cribrosa deformation and scleral canal expansion: independent or related?, Investigative ophthalmology & visual science 52(12) (2011) 9023–9032. [PubMed: 21989723]

[50]. Sigal IA, Grimm J, Schuman JS, Kagemann L, Ishikawa H, Wollstein G, A method to estimate biomechanics and mechanical properties of optic nerve head tissues from parameters measurable using optical coherence tomography, IEEE transactions on medical imaging 33(6) (2014) 1381–1389. [PubMed: 24691117]

[51]. Foong TY, Hua Y, Amini R, Sigal IA, Who bears the load? IOP-induced collagen fiber recruitment over the corneoscleral shell, Experimental Eye Research 230 (2023) 109446. [PubMed: 36935071]

[52]. Jan N-J, Gomez C, Moed S, Voorhees AP, Schuman JS, Bilonick RA, Sigal IA, Microstructural crimp of the lamina cribrosa and peripapillary sclera collagen fibers, Investigative ophthalmology & visual science 58(9) (2017) 3378–3388. [PubMed: 28687851]

[53]. Feola AJ, Coudrillier B, Mulvihill J, Geraldes DM, Vo NT, Albon J, Abel RL, Samuels BC, Ethier CR, Deformation of the lamina cribrosa and optic nerve due to changes in cerebrospinal fluid pressure, Investigative ophthalmology & visual science 58(4) (2017) 2070–2078. [PubMed: 28389675]

[54]. Hua Y, Voorhees AP, Sigal IA, Cerebrospinal fluid pressure: revisiting factors influencing optic nerve head biomechanics, Investigative ophthalmology & visual science 59(1) (2018) 154–165. [PubMed: 29332130]

[55]. Safa BN, Bleeker A, Berdahl JP, Ethier CR, The Effects of Negative Periocular Pressure on Biomechanics of the Optic Nerve Head and Cornea: A Computational Modeling Study, Translational Vision Science & Technology 12(2) (2023) 5–5.

[56]. Sibony PA, Wei J, Sigal IA, Gaze-evoked deformations in optic nerve head drusen: repetitive shearing as a potential factor in the visual and vascular complications, Ophthalmology 125(6) (2018) 929–937. [PubMed: 29361354]

[57]. Fisher LK, Wang X, Tun TA, Chung H-W, Milea D, Girard MJ, Gaze-evoked deformations of the optic nerve head in thyroid eye disease, British Journal of Ophthalmology 105(12) (2021) 1758–1764. [PubMed: 33468490]

[58]. Zarei V, Zhang S, Winkelstein BA, Barocas VH, Tissue loading and microstructure regulate the deformation of embedded nerve fibres: predictions from single-scale and multiscale simulations, Journal of the Royal Society Interface 14(135) (2017) 20170326. [PubMed: 28978743]

[59]. Schwaner SA, Feola AJ, Ethier CR, Factors affecting optic nerve head biomechanics in a rat model of glaucoma, Journal of the Royal Society Interface 17(165) (2020) 20190695. [PubMed: 32228401]

[60]. Grytz R, Downs JC, A forward incremental prestressing method with application to inverse parameter estimations and eye-specific simulations of posterior scleral shells, Computer methods in biomechanics and biomedical engineering 16(7) (2013) 768–780. [PubMed: 22224843]

[61]. Sherman VR, Yang W, Meyers MA, The materials science of collagen, Journal of the mechanical behavior of biomedical materials 52 (2015) 22–50. [PubMed: 26144973]

[62]. Zhang L, Lake S, Barocas V, Shephard M, Picu R, Cross-linked fiber network embedded in an elastic matrix, Soft matter 9(28) (2013) 6398–6405. [PubMed: 24089623]

[63]. Zhang L, Lake SP, Lai VK, Picu CR, Barocas VH, Shephard MS, A coupled fiber-matrix model demonstrates highly inhomogeneous microstructural interactions in soft tissues under tensile load, Journal of biomechanical engineering 135(1) (2013) 011008. [PubMed: 23363219]

[64]. Midgett DE, Jefferys JL, Quigley HA, Nguyen TD, The contribution of sulfated glycosaminoglycans to the inflation response of the human optic nerve head, Investigative Ophthalmology & Visual Science 59(7) (2018) 3144–3154. [PubMed: 30025126]

[65]. Pachenari M, Hatami-Marbini H, Regional differences in the glycosaminoglycan role in porcine scleral hydration and mechanical behavior, Investigative Ophthalmology & Visual Science 62(3) (2021) 28–28.

[66]. Albon J, Karwatowski WS, Easty DL, Sims TJ, Duance VC, Age related changes in the non-collagenous components of the extracellular matrix of the human lamina cribrosa, British Journal of Ophthalmology 84(3) (2000) 311–317. [PubMed: 10684844]

[67]. Safa BN, Peloquin JM, Natriello JR, Caplan JL, Elliott DM, Helical fibrillar microstructure of tendon using serial block-face scanning electron microscopy and a mechanical model for interfibrillar load transfer, Journal of the Royal Society Interface 16(160) (2019) 20190547. [PubMed: 31744419]

[68]. Gogola A, Jan N-J, Brazile B, Lam P, Lathrop KL, Chan KC, Sigal IA, Spatial patterns and age-related changes of the collagen crimp in the human cornea and sclera, Investigative ophthalmology & visual science 59(7) (2018) 2987–2998. [PubMed: 30025116]

[69]. Jan N-J, Sigal IA, Collagen fiber recruitment: a microstructural basis for the nonlinear response of the posterior pole of the eye to increases in intraocular pressure, Acta biomaterialia 72 (2018) 295–305. [PubMed: 29574185]

[70]. Voorhees AP, Jan N-J, Austin ME, Flanagan JG, Sivak JM, Bilonick RA, Sigal IA, Lamina cribrosa pore shape and size as predictors of neural tissue mechanical insult, Investigative ophthalmology & visual science 58(12) (2017) 5336–5346. [PubMed: 29049736]

[71]. Ji F, Yang B, Hua Y, Lee P-Y, Zhu Z, Sigal IA, Characterization of lamina cribrosa beam insertion into the sclera canal in sheep, pig, monkey, and human, Investigative Ophthalmology & Visual Science 61(7) (2020) 4782–4782.

[72]. Sigal IA, Flanagan JG, Lathrop KL, Tertinegg I, Bilonick R, Human lamina cribrosa insertion and age, Investigative ophthalmology & visual science 53(11) (2012) 6870–6879. [PubMed: 22956611]

[73]. Yang H, Williams G, Downs JC, Sigal IA, Roberts MD, Thompson H, Burgoyne CF, Posterior (outward) migration of the lamina cribrosa and early cupping in monkey experimental glaucoma, Investigative ophthalmology & visual science 52(10) (2011) 7109–7121. [PubMed: 21715355]

[74]. Winkler M, Jester B, Nien-Shy C, Massei S, Minckler DS, Jester JV, Brown DJ, High resolution three-dimensional reconstruction of the collagenous matrix of the human optic nerve head, Brain research bulletin 81(2–3) (2010) 339–348. [PubMed: 19524027]

[75]. Ghosh N, Vitkin IA, Tissue polarimetry: concepts, challenges, applications, and outlook, Journal of biomedical optics 16(11) (2011) 110801-110801-29.

[76]. Tuchin VV, Polarized light interaction with tissues, Journal of biomedical optics 21(7) (2016) 071114–071114.

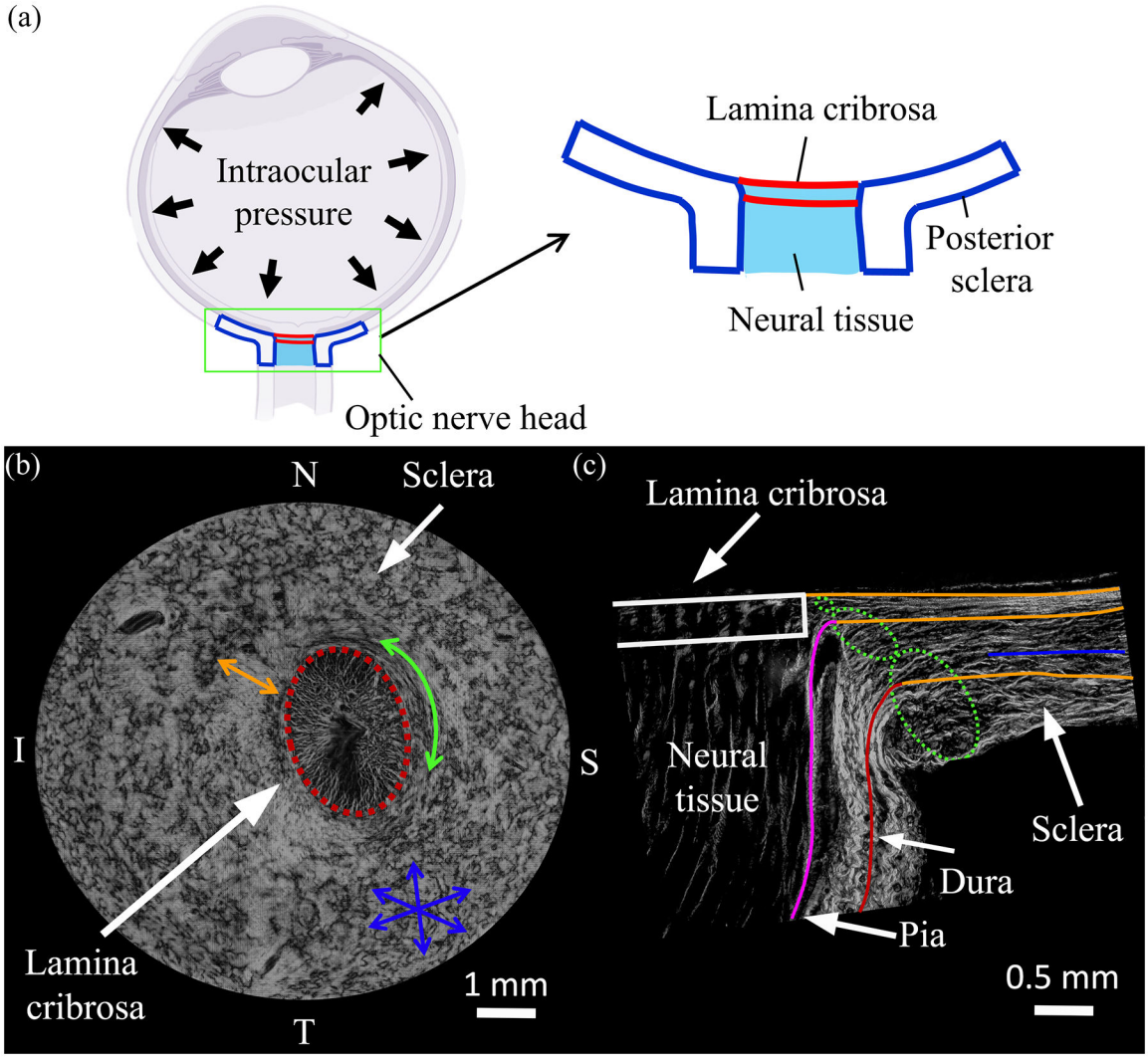

Figure 1.

(a) Schematic of an eye cross-section with a zoomed view of posterior sclera (blue), lamina cribrosa (red), and retrolaminar neural tissue (light blue) regions highlighted at the optic nerve head (ONH). (b) An image of a coronal section through the ONH of a pig eye. The image shown was acquired using polarized light microscopy, such that the brightness of a pixel indicates local retardance, in this case roughly proportional to the collagen in the section plane. Discernible in the image are the lamina cribrosa (red ellipse) surrounded by the sclera. The collagen fibers in the sclera can be classified in three groups [9, 10, 74]: circumferential fiber bundles around the scleral canal, indicated by the green arrow. Radial fiber bundles, indicated by the orange arrow. So-called random fiber bundles located far away from the scleral canal, indicated by the light blue arrows. The pig lamina cribrosa is elliptical, as for humans and monkeys. However, in pigs the long axis is horizontal (N-T axis), whereas in humans and monkeys it is vertical (S-I axis). (c) An image of an axial cross section through the optic nerve head. The image was also acquired using polarized light microscopy, but since the area of interest is smaller than in (a) we are able to discern more details. Also visible is the lamina cribrosa (red) with the adjacent sclera to the right and the

retrolaminar neural tissues beneath. Also discernible are the radial sclera fiber bundles in the innermost sclera (orange), circumferential fiber bundles adjacent to the canal (green), and random fiber bundles (blue) elsewhere. From this perspective circumferential fiber bundles are close to perpendicular to the section, and thus less bright or even dark. It is important to notice the continuous, smooth transition of collagen fiber bundles from the sclera to pia mater and dura mater region.

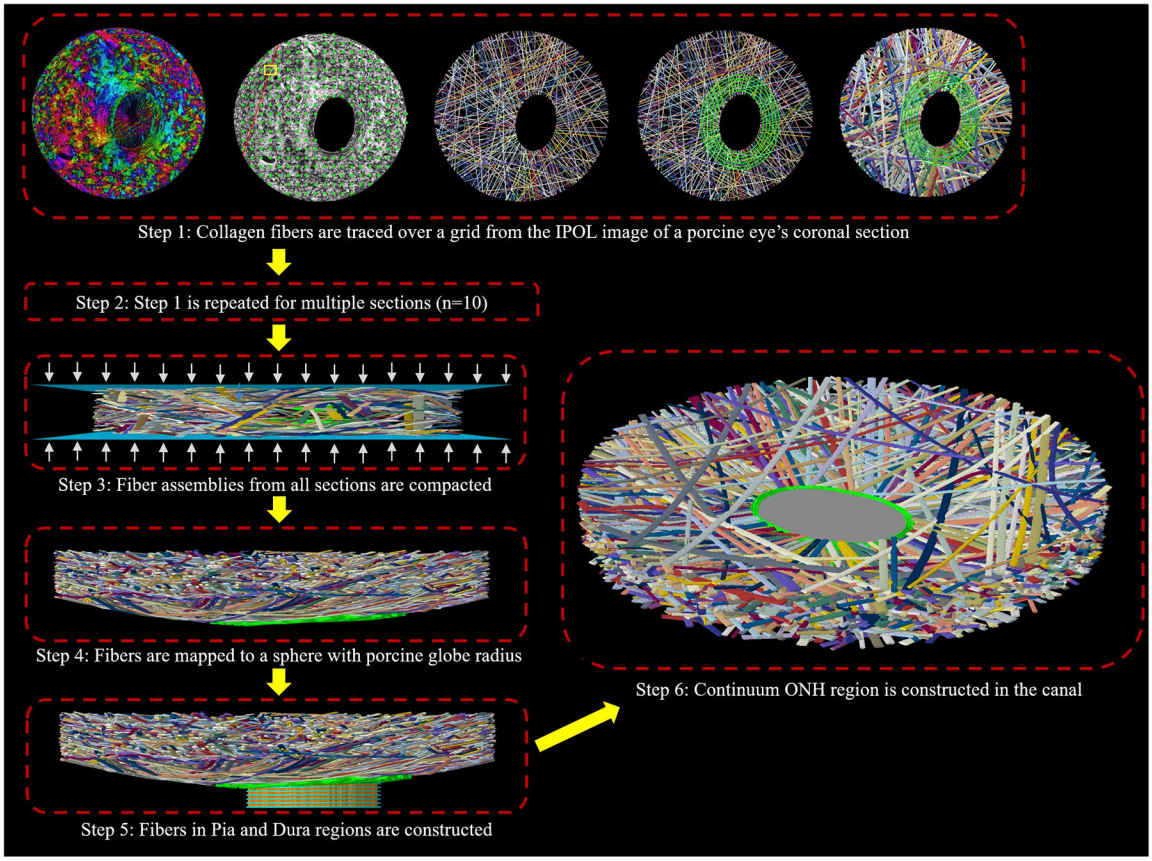

Figure 2.

Schematic representation of the fibrous finite element (FFE) model reconstruction workflow developed in this work. **(a)** Step 1 involved constructing discrete collagen fiber bundles of the sclera part from the multiple PLM images of porcine coronal sections (n=10). The process is illustrated here for a PLM image (a single section). **(a1)** Each PLM image contains pixel-wise fiber orientation information as shown by the color map and orientation wheel. **(a2)** The PLM image was post-processed to distinguish the non-scleral tissues of the canal (elliptical hole in the image), and a set of regularly spaced grid points (green dots) were selected from the scleral part only for tracing fiber bundles. A fiber bundle centerline (red line) was defined at each grid point based on the average orientation of the pixels surrounding the grid point (yellow square) and trimmed at the outer boundary of the section. **(a3)** The fiber bundle centerlines were traced for all the grid points to obtain an assembly of fiber bundle centerlines. The bundle centerlines intersecting the canal (elliptical hole) were trimmed at the canal boundary and grouped as 'radial' fiber bundles. The remaining fiber bundles were grouped as 'random' fiber bundles. This definition of radial and random fiber bundles is different from previous works [10, 19, 41] (see main text in Section 2.1 for more details). **(a4)** The circumferential fiber bundle centerlines were added manually with depth-dependent distributions based on PLM images (see main text in Section 2.1 for more details). **(a5)** The bundle volumes were assigned randomly, but according to the bundle width distribution obtained from the PLM images and a constant thickness for all fiber bundles. An open-source algorithm was used to resolve the inter-penetrations among

fiber bundles. This construction process (a1-a5) was repeated for multiple PLM images or sections. **(b)** In Step 2, the assemblies of fiber bundles from Step 1 were compacted between two rigid plates to obtain a tightly packed fiber assembly. **(c)** In Step 3, the compacted fiber bundles were curved according to the globe radius of a porcine eye. This completes the construction of the fibrous sclera part. **(d)** In Step 4, two subsets of scleral radial fiber bundles were curved down in the posterior direction to construct longitudinal fiber bundles of pia and dura mater parts. We added the circumferential fiber bundles manually in these parts. **(e)** In Step 5, the continuum lamina cribrosa and neural tissue parts in the canal were added to the model. The fiber bundles and their centerlines are shown in random colors for visualization.

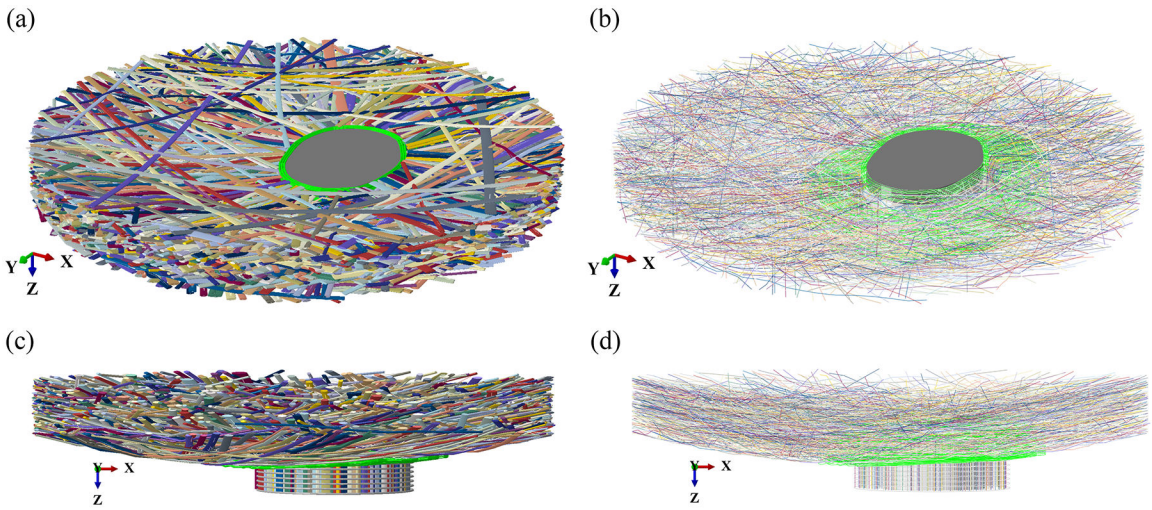

Figure 3.

Perspective views of the FFE model with the fibrous collagen tissues surrounding the continuum parts in the canal. (a) A 3D isometric view with bundle volumes, and (b) A 3D skeletonized view with bundle centerlines. The sagittal views of the FFE model with (c) bundle volumes and (d) skeletonized bundles. The scleral circumferential fiber bundles are colored green, and the remaining bundles are colored randomly for visualization. The continuum lamina cribrosa and neural tissue parts are colored gray.

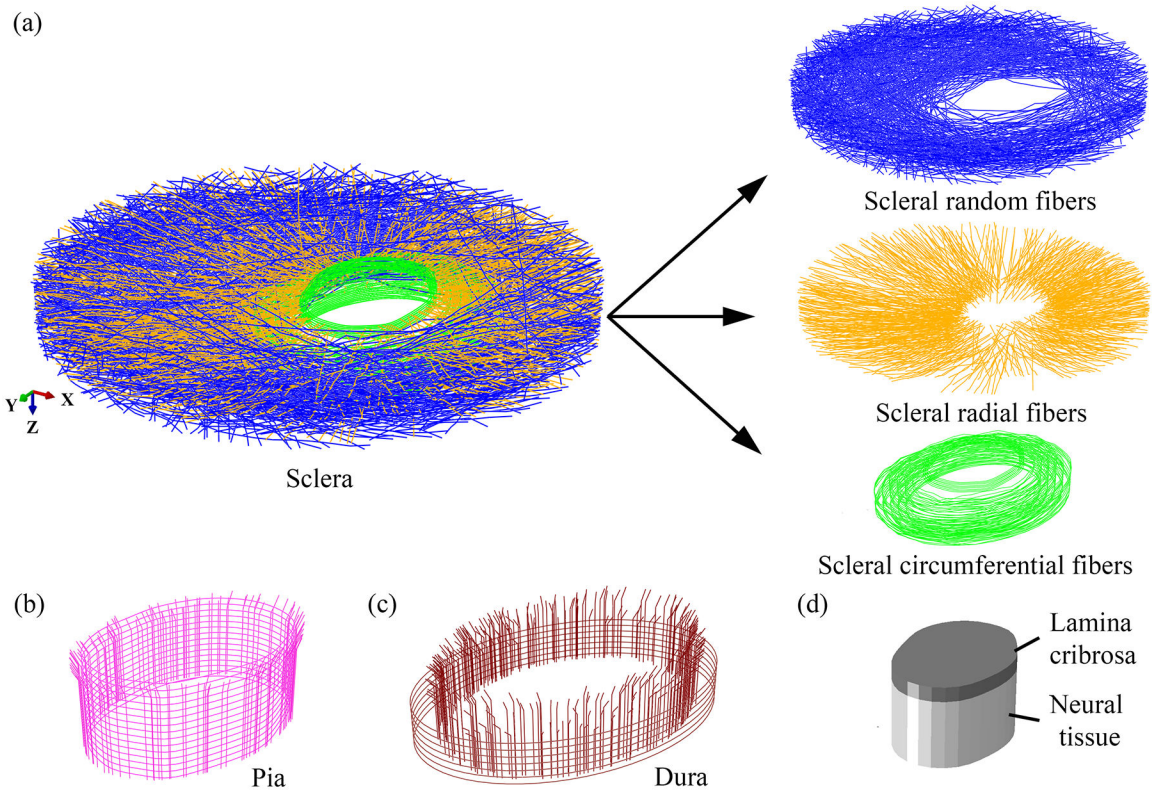

Figure 4.

Isolated views of the various parts in the FFE model. (a) the entire sclera part with random (blue), radial (orange), and circumferential (green) fiber bundles (left) and its isolated fiber bundle groups (right). (b) The pia mater, and (c) the dura mater parts with circumferential and longitudinal fiber bundles. (d) the lamina cribrosa and the neural tissue parts. Fiber bundles are shown using their centerlines only. The parts in (a)-(c) are entirely fibrous, and the parts in (d) are continuum.

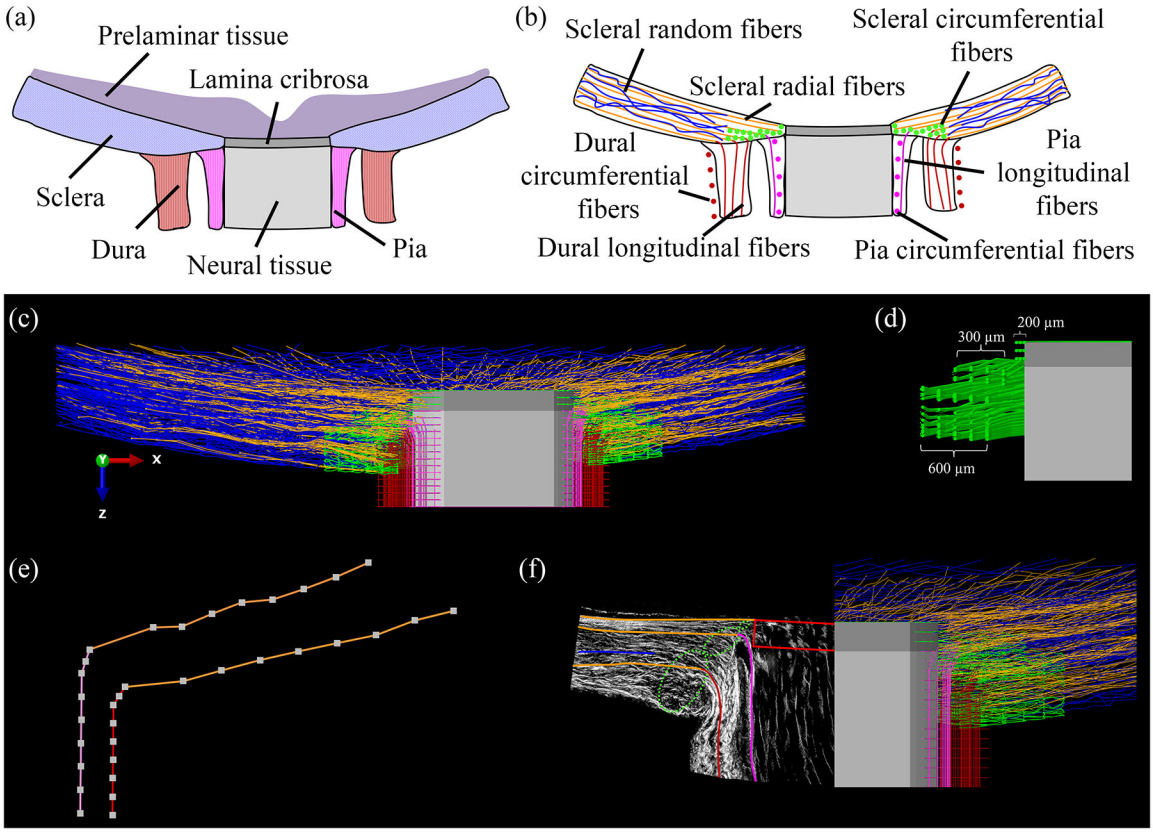

Figure 5.

(a) Schematic of a porcine ONH with various anatomic regions highlighted. (b) Schematic of the connective tissues and canal components of the region in (a) with various collagen fiber bundle groups labeled according to histological observations and as included in the FFE model. (c) Cut-model view of the FFE model along the sagittal plane with various collagen fiber bundle groups in the ONH, continuum lamina cribrosa, and continuum neural tissue parts. (d) Partial view of the FFE model showing the distribution of circumferential fiber bundles with respect to the canal tissues (see the main text for details). (e) Two representative collagen fiber bundles that are continuous from the sclera to pia and dura maters. The symbols (squares) represent the finite element nodes, indicating the continuity of the bundle across different tissues. (f) Qualitative comparison of the cross-sections observed in PLM (left) and the FFE model (right). The colors in (c) to (f) indicate the various groups of fiber bundles: scleral radial bundles in orange, scleral random bundles in blue, scleral circumferential bundles in green, pia bundles in magenta, and dura bundles in maroon. For visualization we show only the fiber bundle skeletons in (c) and (f). It would be impossible to see into the model if the bundles were shown with full thickness, as in Fig. 3. The histological image shown in (f) was acquired using polarized light microscopy, such that the brightness of a pixel indicates measured local retardance. The local retardance will be low if the amount of collagen is low, for instance where there is no tissue or if the tissue is not birefringent. However, there are several other factors which can affect the observed retardance [75, 76]. Retardance can be low if there are many fibers with different orientations crossing at a location. Retardance can also be low if the fibers are oriented

perpendicular to the direction of observation, or it can be low if something blocks light from being transmitted across the sample, such as pigment. Conversely, high retardance is likely a good indicator of substantial well-aligned in-plane collagen.

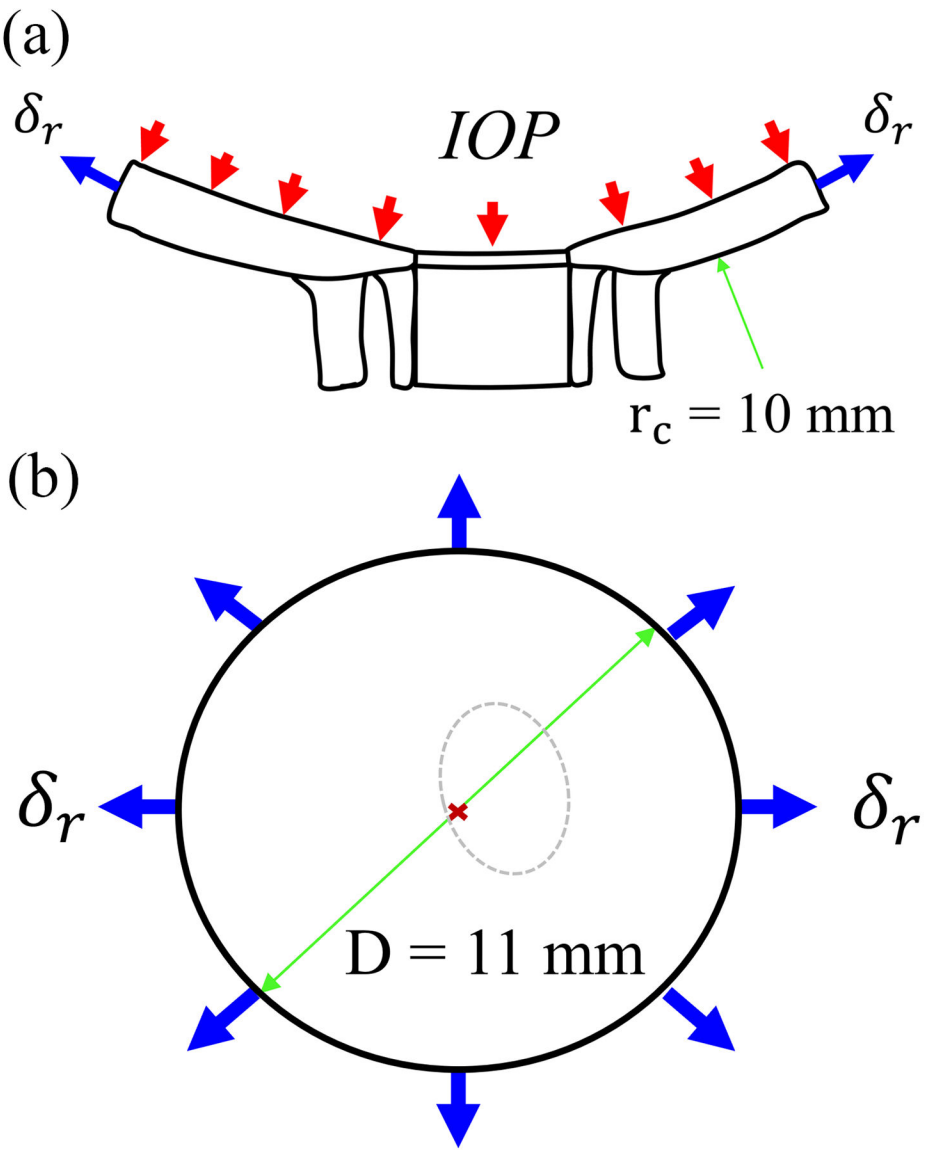

Figure 6.

The boundary conditions applied to the FFE model to simulate an inflation experiment. (a) A pressure boundary condition (equivalent to the IOP range from 0 mmHg to 30 mmHg) was applied on the anterior surface of the model. See the main text for details on the application of the IOP to the fibrous model. (b) A radial displacement boundary condition with respect to the center (red 'x') of the sclera was applied on the outer periphery of the sclera part in the model. The dashed ellipse shows the location of the canal. The black circle indicates the outer boundary of the sclera part.

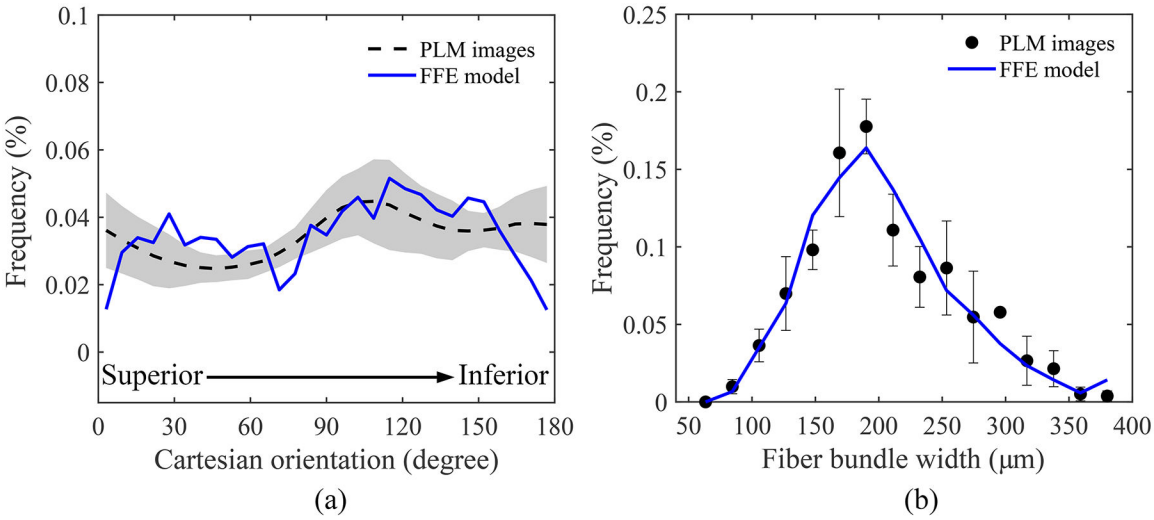

Figure 7.

Structural validation of the FFE model. (a) the comparison of the coronal fiber orientation distributions as measured from the PLM images (dashed line) and the FFE model (solid line). The grey-shaded region represents the standard deviation of fiber orientation from multiple coronal sections of a porcine eye (n=10). (b) the comparison of the width distributions of collagen fiber bundles as measured from the PLM images (symbols) and the FFE model (solid line). The error bars in (b) represent the standard deviation of measurements from multiple sections (n=5).

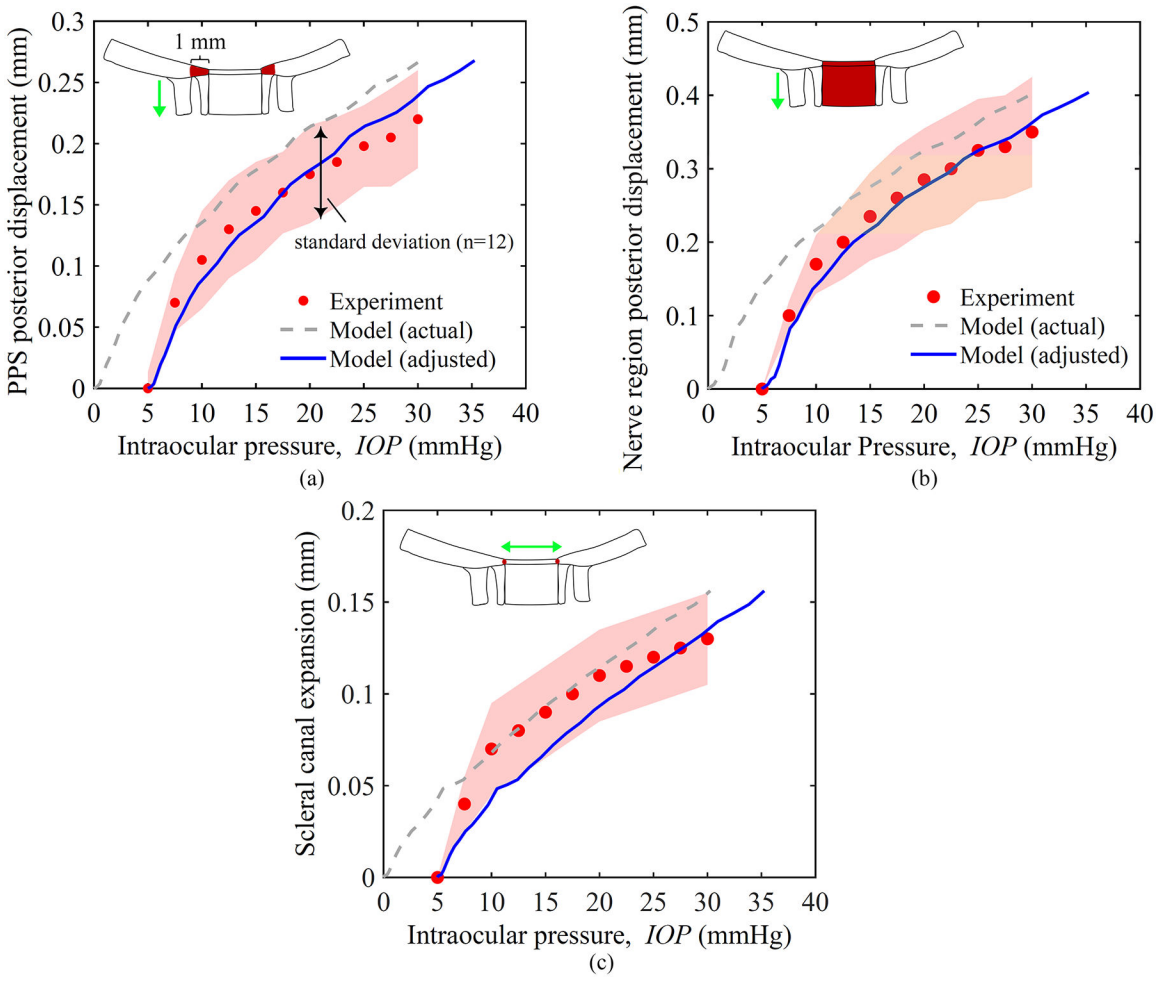

Figure 8.

Mechanical validation of the FFE model. The comparisons of (a) the mean posterior displacement of the porcine peripapillary sclera (PPS), (b) the mean posterior displacement of the optic nerve region (lamina cribrosa and neural tissue parts), and (c) the mean scleral canal expansion between the inflation experiments (symbols) from ref. and the FFE model (lines). The experimental data is adapted from [45]. The model responses are adjusted by 5 mm Hg in the IOP axis to ensure one-to-one comparisons with the experiments. The ONH deformations were measured in the experiments using the specimen configurations at 5 mmHg as the undeformed configuration. The configuration at 0 mmHg was used as the undeformed configuration in the model (see Section 3.2 for further details). The shaded regions in (a)-(c) represent the standard deviation of experimental measurements for multiple porcine eyes (n=12) [45]. The dashed lines in (a)-(c) represent the actual responses of the FFE model, and the solid lines represent the adjusted responses of the FFE model. The schematics in (a)-(c) indicate the regions used for calculating the mean posterior displacements and the canal expansion.

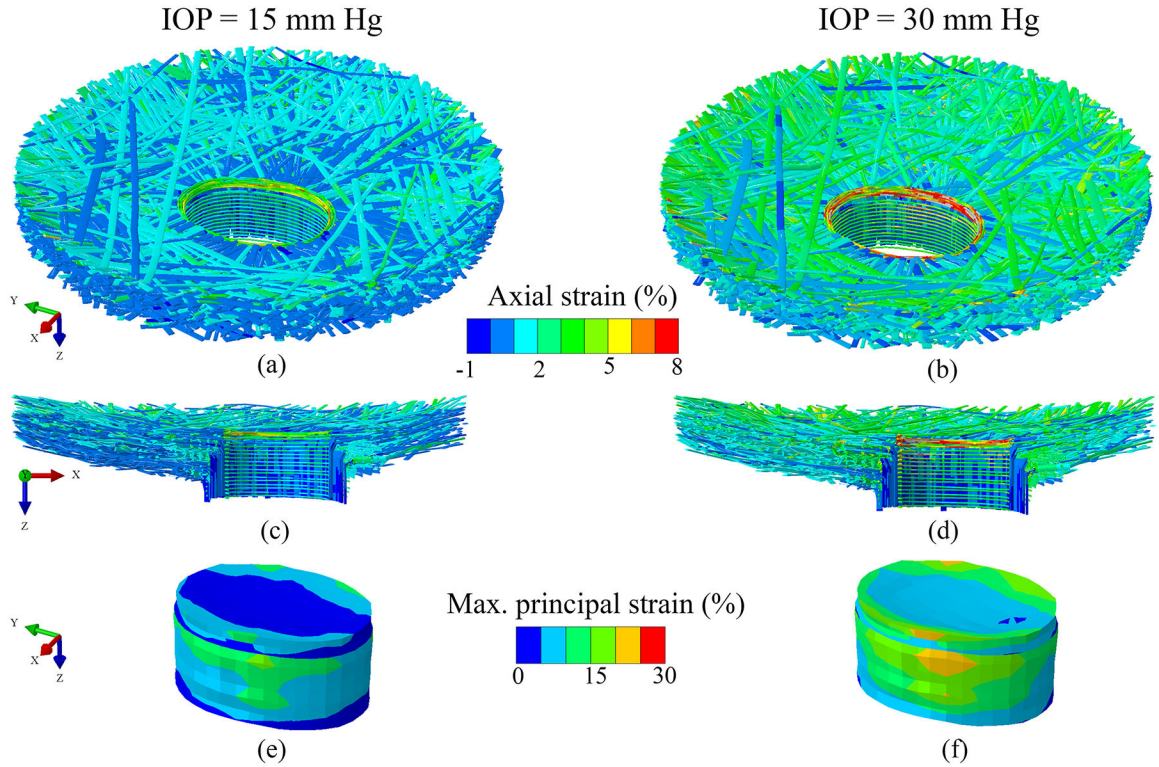

Figure 9.

Strain contour plots of the fibrous and the continuum parts in the FFE model at normal (IOP = 15 mm Hg, left column) and elevated (IOP = 30 mm Hg, right column) IOP levels. The 3D isometric views of the fibrous parts with the contour plots of axial strain along the length of individual fiber bundles at (a) normal and (b) elevated IOP levels. The cut-model views of the fibrous parts along the inferior-superior direction with the axial strain contour plots at (c) normal and (d) elevated IOP levels. The 3D isometric views of the continuum parts of the FFE model with the maximum principal strain contour plots at (e) normal and (f) elevated IOP levels.

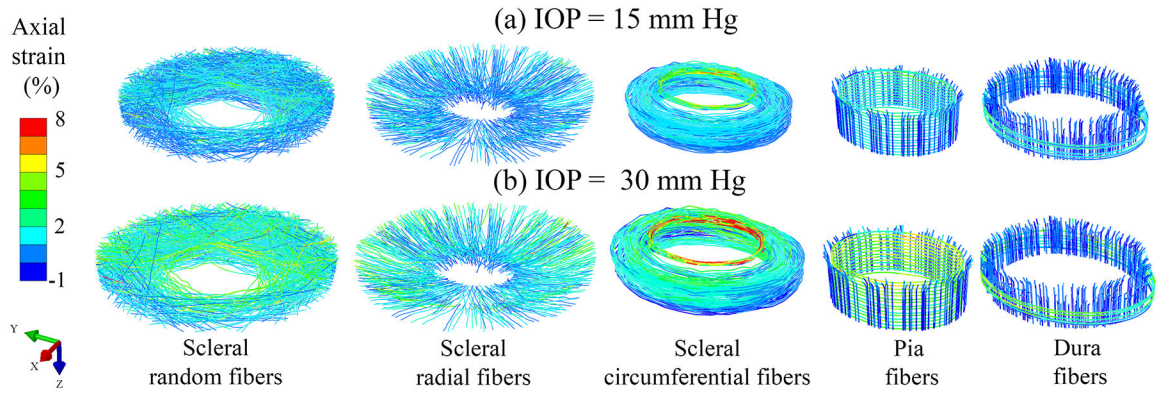

Figure 10.

Strain contour plots of various fiber bundle groups in the FFE model at (a) normal (IOP = 15 mmHg, top row) and (b) elevated (IOP = 30 mmHg, bottom row) IOP levels. The first three columns correspond to the scleral random, radial, and circumferential fiber bundle groups, respectively. The fourth and fifth columns correspond to the fiber bundle groups of the pia and the dura mater parts, respectively.

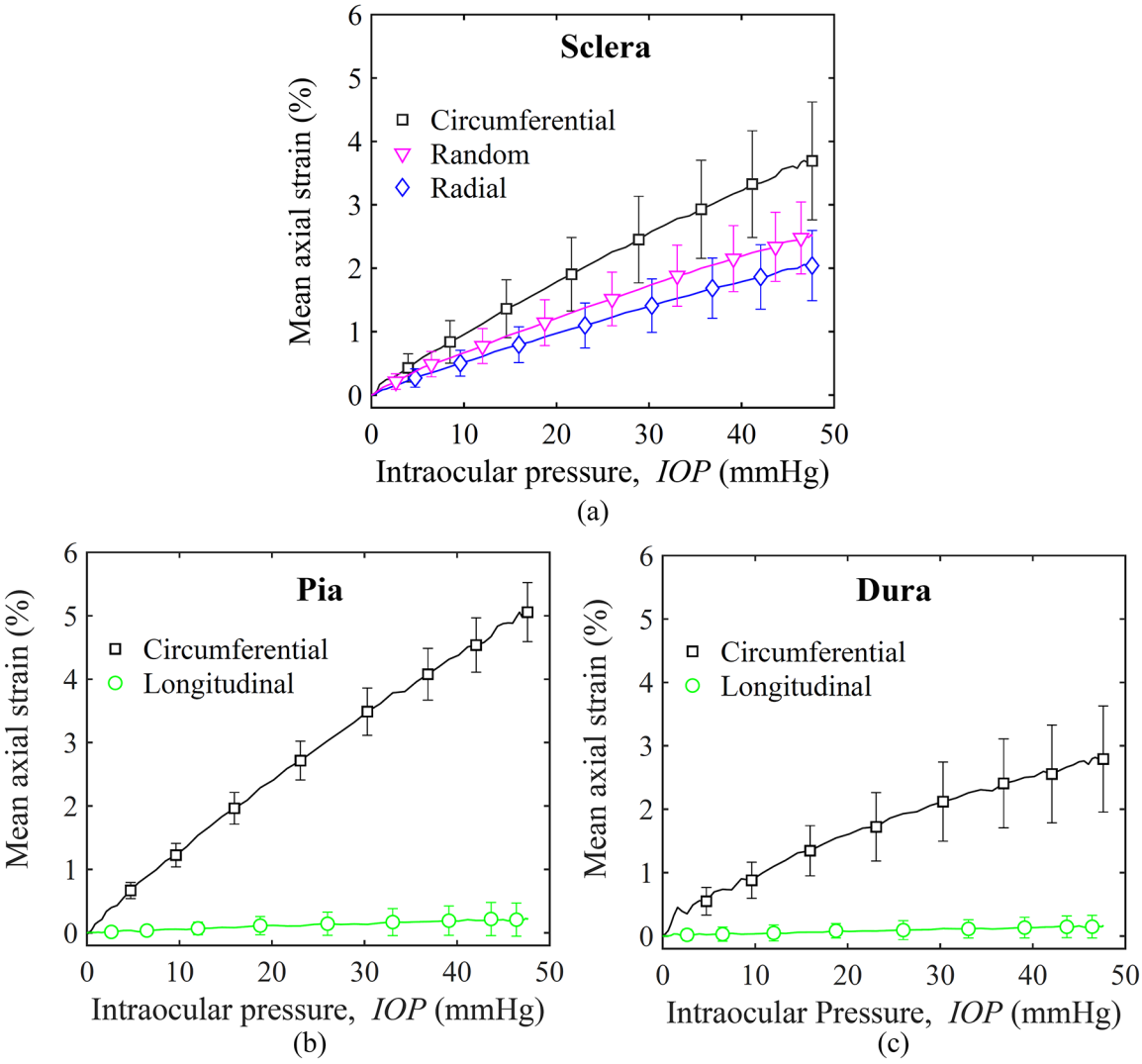

Figure 11.

Variation of the mean axial strain of individual fiber bundles with IOP for various fiber bundle groups of the (a) sclera, (b) pia mater, and (c) dura mater parts in the FFE model. The error bars represent the standard deviation of the mean axial strain over all bundles of the same group.

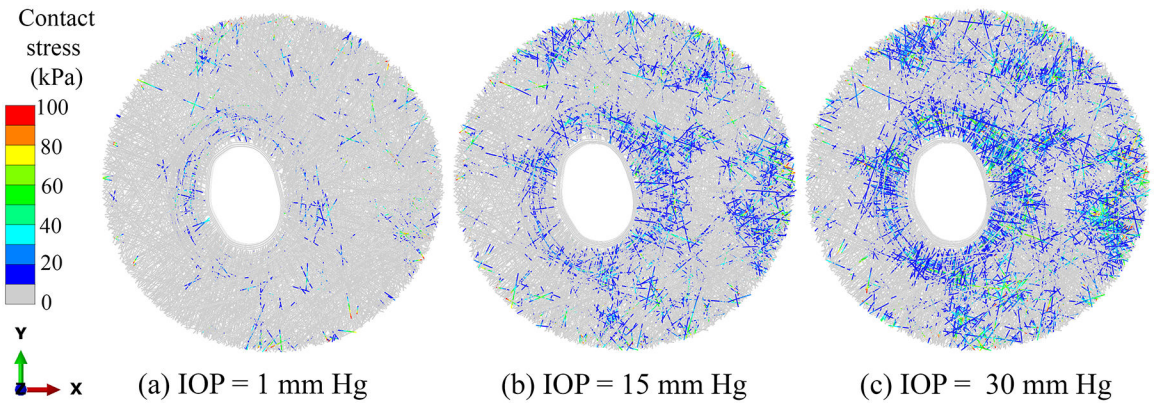

Figure 12.

Contour maps of the contact stress between bundle segments at different IOP labels. (a) IOP = 1 mmHg (0.13 kPa), (b) IOP = 15 mmHg (1.99 kPa), and (c) IOP = 30 mmHg (3.99 kPa). To provide a sense of scale, a contact stress of 100 kPa is equal to 750 mmHg. The interactions between fibers give rise to localized contact stresses in the bundle segments which can be significantly larger than the applied IOP.